Acta Pharmaceutica Sinica B 2021;11(3):781−794

Chinese Pharmaceutical Association
Institute of Materia Medica, Chinese Academy of Medical Sciences

Acta Pharmaceutica Sinica B

www.elsevier.com/locate/apsb
www.sciencedirect.com

ORIGINAL ARTICLE

Design, synthesis and biological evaluation of pyrazolo[3,4-*d*]pyridazinone derivatives as covalent FGFR inhibitors

Xiaowei Wu[a,†], Mengdi Dai[b,c,†], Rongrong Cui[d,†], Yulan Wang[a], Chunpu Li[a], Xia Peng[b], Jihui Zhao[a,c], Bao Wang[a], Yang Dai[b], Dan Feng[a], Tianbiao Yang[a], Hualiang Jiang[a,d], Meiyu Geng[b], Jing Ai[b,c,*], Mingyue Zheng[a,c,d,*], Hong Liu[a,*]

[a]*State Key Laboratory of Drug Research, Shanghai Institute of Materia Medica, Chinese Academy of Sciences, Shanghai 201203, China*
[b]*Division of Anti-Tumor Pharmacology, State Key Laboratory of Drug Research, Shanghai Institute of Materia Medica, Chinese Academy of Sciences, Shanghai 201203, China*
[c]*University of Chinese Academy of Sciences, Beijing 100049, China*
[d]*School of Chinese Materia Medica, Nanjing University of Chinese Medicine, Nanjing 210023, China*

Received 2 June 2020; received in revised form 23 July 2020; accepted 24 August 2020

KEY WORDS

Tyrosine kinase;
Covalent FGFR inhibitors;
Virtual screening;
Pyrazolo[3,4-*d*] pyridazinone;
Structure−activity relationships;
Antitumor efficacy

Abstract Fibroblast growth factor receptors (FGFRs) have emerged as promising targets for anticancer therapy. In this study, we synthesized and evaluated the biological activity of 66 pyrazolo[3,4-*d*]pyridazinone derivatives. Kinase inhibition, cell proliferation, and whole blood stability assays were used to evaluate their activity on FGFR, allowing us to explore structure−activity relationships and thus to gain understanding of the structural requirements to modulate covalent inhibitors' selectivity and reactivity. Among them, compound **10h** exhibited potent enzymatic activity against FGFR and remarkably inhibited proliferation of various cancer cells associated with FGFR dysregulation, and suppressed FGFR signaling pathway in cancer cells by the immunoblot analysis. Moreover, **10h** displayed highly potent antitumor efficacy (TGI = 91.6%, at a dose of 50 mg/kg) in the FGFR1-amplified NCI-H1581 xenograft model.

Abbreviations: BTK, brutons tyrosine kinase; CADD, computer-aided drug design; EGFR, epidermal growth factor receptor; FGFR, fibroblast growth factor receptor; GSH, glutathione; MAPK, mitogen-activated protein kinase; PI3K, phosphoinositide 3-kinase; PLCγ, phospholipase Cγ; PK, pharmacokinetics; RTKs, receptor tyrosine kinases; SAR, structure−activity relationship.

*Corresponding authors. Tel.: +86 21 50807042 (Hong Liu); +86 21 50271399 (Mingyue Zheng); +86 21 50806600 2413 (Jing Ai).
E-mail addresses: jai@simm.ac.cn (Jing Ai), myzheng@simm.ac.cn (Mingyue Zheng), hliu@simm.ac.cn (Hong Liu).
[†]These authors made equal contributions to this work.

Peer review under responsibility of Chinese Pharmaceutical Association and Institute of Materia Medica, Chinese Academy of Medical Sciences.

https://doi.org/10.1016/j.apsb.2020.09.002

1. Introduction

The development of small-molecule inhibitors targeting tyrosine kinase receptors is one of the hot spots for targeted anticancer therapies[1,2]. The family of fibroblast growth factor receptors (FGFRs) includes four highly conserved transmembrane tyrosine kinase receptors (FGFRs 1−4)[3]. Fibroblast growth factor (FGF) ligands conjugated to FGFRs would induce the dimerization and tyrosine phosphorylation of FGFRs, which further initiates the activation of PI3K/Akt, Ras/MAPK, and PLCγ downstream signaling pathways, etc.[4,5]. The physiological roles of FGF/FGFR signaling involve embryonic development, wound healing, angiogenesis, and tissue cross-talk, etc.[6]. Moreover, FGF/FGFR signaling is critical for cell proliferation, migration, differentiation, apoptosis, and survival[7]. Studies suggest that aberrant FGF/FGFR signaling is closely related to the pathogenesis of a variety of cancers including lung cancers, gastric cancer, breast cancers, ovarian cancers, urothelial cancers, and endometrial cancers, etc.[8−11]. Due to the vital characters of FGF/FGFR signaling, FGFRs have currently emerged as promising targets for anticancer therapy[12].

To date, small-molecule FGFR inhibitors can be divided into two major classes based on their target specificities, including multi-target FGFR inhibitors and selective FGFR inhibitors. Although multi-target FGFR inhibitors can simultaneously inhibit a number of tyrosine kinase receptors, they usually display diverse side effects[13]. Currently, pharmaceutical community has an increasing interest in developing selective FGFR inhibitors with high potency and specificity[14−22]. Debio-1347, AZD-4547, and BGJ-398 (infigratinib) are potent and selective FGFR1/2/3 inhibitors currently under clinical investigations[15−17]. In addition, BAY1163877 (rogaratinib), JNJ-42756493 (erdafitinib), ASP5878, LY2874455, and INCB054828 are highly potent pan-FGFR inhibitors for the treatment of cancer, which are developed by Bayer, Janssen, Astellas, Lilly, and Incyte, respectively[18−22]. Among them, erdafitinib has been approved by the U.S. Food and Drug Administration (FDA) for the treatment of urothelial cancer and metastatic urothelial carcinoma.

In recent years, covalent receptor tyrosine kinase (RTK) inhibitors have attracted intensive attention from pharmaceutical industry and academic institutions. Generally, covalent kinase inhibitors which contain a "warhead" (reactive functional group) can improve binding affinity and selectivity by forming covalent interaction with a certain residue of the target kinase. Moreover, covalent kinase inhibitors could display better performance against drug resistance caused by mutations when compared to non-covalent inhibitors. Therefore, it's promising and urgent to develop covalent inhibitors. More recently, a number of covalent FGFR inhibitors have been reported, which are considered as the next-generation FGFR inhibitors, and some of them are in clinical trials[23−31]. As summarized in Fig. 1, covalent pan-FGFR inhibitors PRN1371 (phase I), FIIN-3, and TAS-120 (phase I/II) can form a covalent bond with a cysteine residue in the phosphate-binding loop (P-loop) of FGFR[24,27,30]. FGFR4-specific inhibitors BLU554 (phase I), H3B-6527 (phase I), and FGF401 (phase I/II) bind to the Cys552 residue that is located in the hinge region of FGFR4, which leads to better potency against FGFR4 than other FGFR1/2/3 because Cys552 residue is not conserved in FGFR1/2/3[25,28,31]. Recently, several covalent RTK inhibitors osimertinib (EGFR)[32], afatinib (EGFR)[33], and ibrutinib (BTK)[34] have been approved by FDA because of their good efficiency and favorable safety profile in clinical trials. Considering the wide range of implications of FGFRs in oncogenesis, the scaffolds of covalent FGFR inhibitors are still limited, and there remains an urgent need to develop novel FGFR inhibitors with good efficiency and safety profile.

In our previous study, we developed a machine-learning based on FGFR specific scoring function RTKscore, and successfully identified a novel pyrazolo[3,4-*d*]pyridazinone compound **1** by applying RTKscore to virtual screening of FGFR inhibitors against a commercial compound library[35]. Compound **1** showed good activity against FGFR1 (IC_{50} = 114.5 nmol/L), but the cellular activity against KG-1 cell was only at micromolar level. To explore the structure−activity relationships (SARs), a series of derivatives of compound **1** have been designed, synthesized, and bio-evaluated anti-FGFR activities *in vitro*. As shown in Fig. 2, the co-crystallographic study (PDB id: 6ITJ)[35] has revealed that the interactions between FGFR and the pyrazolo[3,4-*d*]pyridazinone scaffold derivatives can be divided into three parts: (1) the pyridazinone moiety forms three H-bonds with residues Ala564 and Glu562 in the hinge region; (2) the benzofuran ring stretches into the hydrophobic pocket; and (3) the phenyl group is oriented to the P-loop region. It's worth mentioning that the cysteine residue in P-loop region provides an opportunity for designing covalent FGFR inhibitors. Our previous study has confirmed that introducing an acrylamide substituent on the phenyl ring may significantly improve the cellular potency and selectivity toward FGFRs. In the current study, we aim to fully explore the SARs of the pyrazolo[3,4-*d*]pyridazinone scaffold and to investigate the *in vivo* antitumor activity of these derivatives.

2. Results and discussion

2.1. Chemistry

Lead optimization was initiated with the aim of identifying compounds with enhanced potency and pharmacokinetics (PK) properties suitable for *in vivo* evaluation. To explore the SAR of the pyrazolo[3,4-*d*]pyridazinone scaffold, we designed and synthesized three series of derivatives. The desired compounds were prepared according to the following synthetic routes as shown in Schemes 1−5. Commercially available compounds **11** were reacted with ethyl bromoacetate to afford various benzofuran derivatives **12a**−**12t** (Scheme 1). Compounds **13** were synthesized by heating the esters **12** and acetonitrile in the presence of sodium hydride in anhydrous THF (Schemes 1 and 2). The treatment of anilines **14** with sodium nitrite in hydrochloric acid solution afforded diazonium salts, then followed by the addition of ethyl 2-chloroacetoacetate to provide hydrazonoyl chlorides **15a**−**15v**. Benzyl chlorides **16a**−**16d** were reacted with hydrazine hydrate, which were followed by the addition of ethyl glyoxylate giving

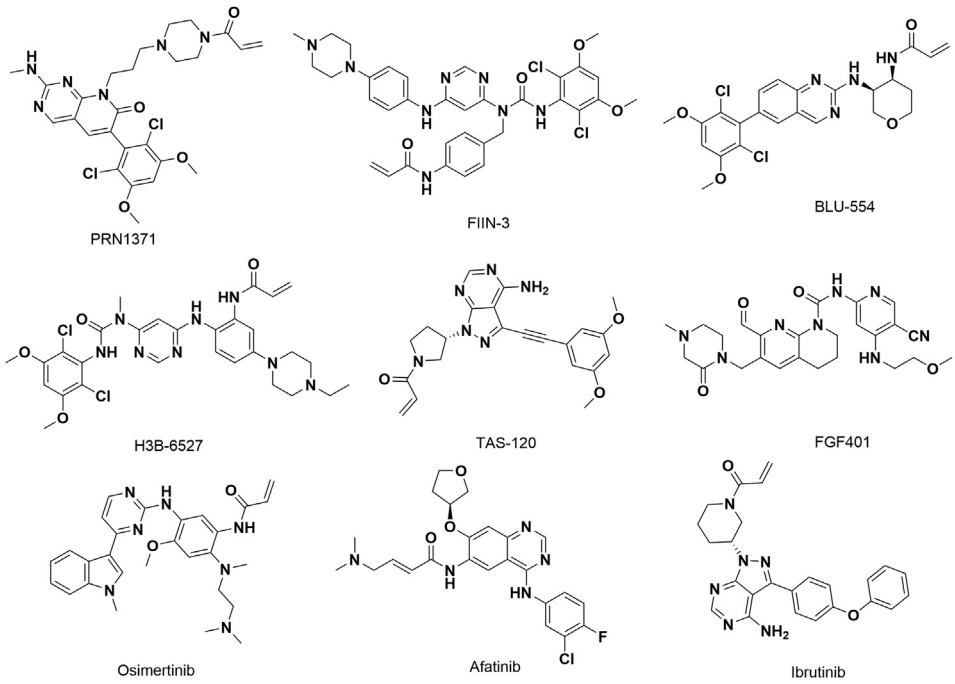

Figure 1 The structures of covalent small-molecule inhibitors.

compounds **17a**−**17d** (Scheme 2). The hydrazonoyl chlorides (**15w**−**15z**) were obtained by the chlorination of **17a**−**17d** with *N*-chlorosuccinimide. The cyclization reaction of compounds **13** with hydrazonoyl chlorides **15** gave the intermediates **I1**−**I49**. The reaction of **I1** with hydrazine hydrate in ethanol at 80 °C afforded compound **3**. The corresponding products **1**, **2** and **4**−**9** were obtained by cyclization of intermediates **I1**−**I49** with hydrazine hydrate under microwave heating. Coupling reaction of the pyrazole **I42** with different alkyl amines produced the corresponding compounds **I50**−**I53**, which were followed by cyclization reaction giving compounds **9x**−**9za** (Scheme 2). Compounds **10c** and **10d** were prepared from reduction of **9m** and followed by acylation with the corresponding acyl chlorides **20** (Scheme 3). The reaction of compound **9nd** with *N*,*N*,*N*-trimethylethylenediamine under microwave afforded **9ne**. The nitro group in compounds **9n**, **9na**, **9nb**, **9nc**, and **9ne** underwent reduction and acylation subsequently to provide the desired products **10a**, **10b**, and **10e**−**10m**.

2.2. *SARs of the pyrazolo[3,4-d]pyridazinone scaffold*

According to the interactions of compound **1** with FGFR1, the pyridazinone moiety can form three H-bonds with Ala564 and Glu562, and the benzofuran ring stretches into the hydrophobic pocket (Fig. 3). Therefore, we initially investigated the influence of pyrazolo[3,4-*d*]pyridazinone part to activity (Table 1). When the pyridazinone moiety was replaced with a pyridazin ring or a carbohydrazide group (compounds **2** and **3**), these two compounds exhibited decreased inhibitory activities against FGFR1. The results indicated that pyrazolo[3,4-*d*]pyridazinone scaffold which forms three hydrogen bonds with the amino acid residues plays a critical role in keeping inhibitory activities. Then, replacement of the benzofuran moiety with benzothiophene, benzene or furan would also result in reduced potency against FGFR1 dramatically (compounds **4**−**7**).

Since the pyrazolo[3,4-*d*]pyridazinone scaffold and the benzofuran motif are important for maintaining inhibitory

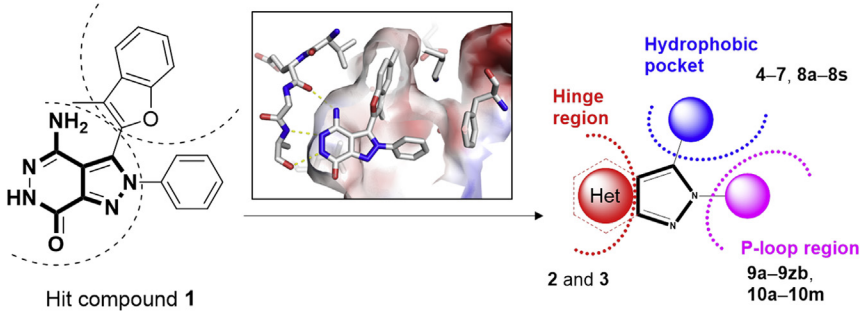

Figure 2 SAR exploration of pyrazolo[3,4-*d*]pyridazinone derivatives guided by X-ray crystallography (PDB id: 6ITJ)[35]. Electrostatic potential surface of ligand binding pocket was generated with PyMOL.

activities against FGFRs, we started to focus the SAR work on the benzofuran moiety which is located at the hydrophobic pocket. We synthesized various pyrazolo[3,4-*d*]pyridazinone analogues with various substituted benzofurans (**8a**–**8s**). Table 2 summarized the SAR of substituents on the benzofuran moiety with respect to inhibition of FGFR1 kinase activity. First, we investigated the substituents at the C-3 position of benzofuran ring; compounds **8a** and **8b** were prepared. When methyl group at the C-3 position was changed to hydrogen or ethyl group, the inhibitory activity of these compounds reduced significantly relative to compound **1**. Subsequently, introduction of fluorine at the C-4 position (**8c**) also led to decreased inhibitory potency. Interestingly, some hydrophobic groups such as methoxyl, methyl, and halogens were introduced at the C-5 or C-6 position of benzofuran moiety (**8d**–**8m**), which maintained or slightly increased the inhibitory potency against FGFR. Notably, trifluoromethyl group at the C-5 position (**8n**) would lead to weaker inhibitory activity, which was probably due to the strong electronegativity of trifluoromethyl group. In addition, analogues with methyl group or chlorine at the C-7 position of benzofuran moiety (**8o**–**8q** and **8s**) resulted in significant decrease of inhibitory activities compared to compound **8g**. The reason for the loss of inhibitory activities was probably that large substituents at the C-7 position provided an unfavorable interaction with the residues in the hydrophobic pocket. Introduction of a smaller fluorine atom at the C-7 position would have a marginal impact on potency (**8r**).

With the optimized benzofuran ring, we put our attention on the phenyl moiety of compound **8g**. As summarized in Table 3, introduction of various hydrophobic groups (such as methyl, halogens, isopropyl, and methoxyl) at the C-4 position of benzene ring (**9a**–**9f**) enhanced inhibitory potency against FGFR1 relative to the unsubstituted compound **8g**. Incorporation of *t*-Bu group at the C-4 position (**9g**) or fluorine at the C-3 position (**9h**) would maintain the activity. Additionally, we also investigated the influence of methylsulfonyl, different amides, and nitro groups to the inhibitory potency (**9i**–**9o**). The enzymatic assay suggested that the inhibitory activities of these compounds were maintained or slightly decreased. Interestingly, difluoro-substituted analogue **9p** exhibited improved potency, whereas dichloro-substituted analogue **9q** showed weaker molecular potency probably due to steric hindrance. The analogues **9r** and **9s** also did not exhibit better activities. Replacement of phenyl group in compound **8g** with benzyl group derivatives provided analogues **9t**–**9w**. The inhibitory potency of **9t** was similar to **8g**, while compounds **9u**–**9w** were much less potent than **8g**. Considering the phenyl group stretches toward a solvent area, we tried to attach some soluble chains to the phenyl group to improve the inhibitory potency. Thus, we synthesized analogues (**9x**–**9za**) containing an alkyl amine sidechain for biological testing. However, these compounds did not show obviously increased potency against FGFR.

Based on the preliminary results of enzymatic inhibition assays, we chose compounds **8g**–**8i**, **8m**, **9a**, **9c**, **9e**, **9i**, and **9z** with good enzymatic activities for further evaluating the cellular potency. As shown in Table 4, these compounds did not exhibit good

Table 1 SAR exploration in the hinge region and hydrophobic pocket.

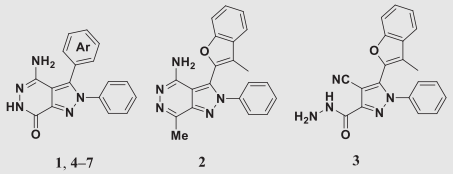

Compd.	Ar	FGFR1 inhibition rate (%)		
		1 μmol/L	0.1 μmol/L	0.01 μmol/L
1	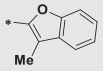	97.4	57.2	–
2	–	–	31.8	–
3	–	12.4	–	–
4		64.7	2.2	0
5		42.7	2.0	0.6
6		22.9	19.6	18.6
7		19.9	20.4	22.9
AZD4547 IC_{50} (nmol/L)		0.8 ± 0.1		

Values are the mean ± SD of two independent assays.
–Not applicable.

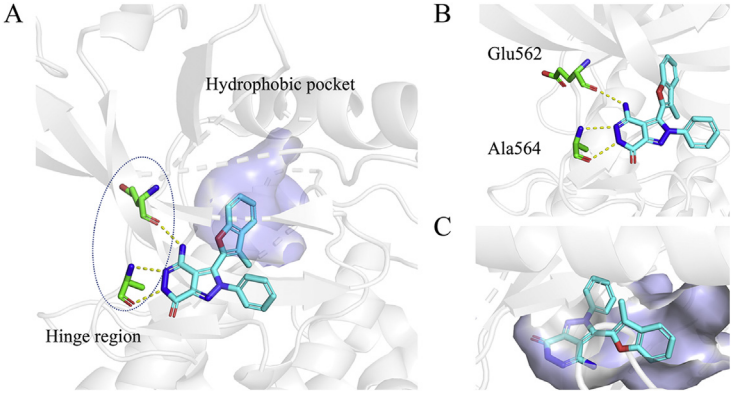

Figure 3 (A) Overall binding interactions of **1** with FGFR1 (6ITJ, PDB). (B) Highlighting the interactions of compound **1** with hinge region in FGFR1. (C) The location of compound **1** benzofuran ring in FGFR1. Electrostatics surface representation defines the shape and extent of hydrophobic pocket in FGFR1.

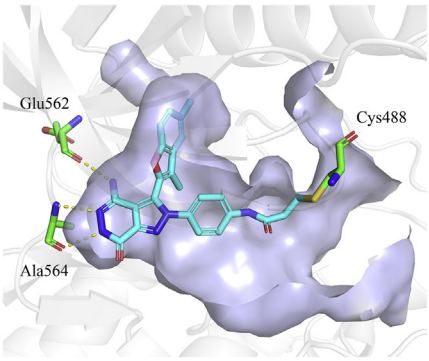

Figure 4 Putative binding modes of compound **10a** (cyan) with FGFR1 (6ITJ, PDB). The relevant interaction residues are shown as sticks (green), the binding pocket depicted as surface.

Table 2 SAR of substituents on the benzofuran moiety.

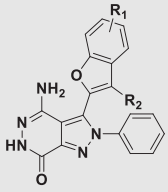

8a–8s

Compd.	R_1	R_2	FGFR1 IC_{50} (nmol/L)
8a	H	H	−11.8%@0.1 μmol/L
8b	H	Et	0%@0.1 μmol/L
8c	4-F	Me	11.0%@0.1 μmol/L
8d	6-MeO	Me	67.7 ± 3.9
8e	5-F	Me	55.7%@0.1 μmol/L
8f	5-MeO	Me	77.5 ± 14.7
8g	5-Me	Me	47.2 ± 12.6
8h	6-F	Me	60.3 ± 10.9
8i	6-Cl	Me	64.2%@0.1 μmol/L
8j	5-Cl	Me	56.4 ± 15.8
8k	6-Me	Me	79.0 ± 12.6
8l	5-Me, 6-Cl	Me	109.9 ± 27.0
8m	5-Br	Me	66.8 ± 16.5
8n	5-CF_3	Me	38.0%@0.1 μmol/L
8o	5,7-Me	Me	16.8%@0.1 μmol/L
8p	7-Cl	Me	38.1%@0.1 μmol/L
8q	4,7-Cl	Me	25.9%@0.1 μmol/L
8r	7-F	Me	78.6%@0.1 μmol/L
8s	7-Me	Me	17.8%@0.1 μmol/L
AZD4547	−	−	0.8 ± 0.1

Values are the mean ± SD of two independent assays.
−Not applicable.

inhibitory potency against the proliferation of FGFR2 amplification SNU16 cell line compared to positive control AZD4547.

In order to improve the cellular activities of compounds, we further optimized the phenyl group on **8f**, **8g**, **8h** and **8m**. As previously reported[35], the acrylamide attached to the benzene ring binds covalently to the residue Cys488 (Fig. 4). A series of analogues with acrylamides were prepared for biological assays. As shown in Table 5, compound **10a** (R_1 = 5-Me) exhibited highly potent inhibition activity against the FGFR1 kinase (IC_{50} = 4.8 nmol/L). To our delight, **10a** inhibited the proliferation of the FGFR2-dependent SNU16 cell line potently with an IC_{50} value of 2.5 nmol/L. Additionally, we added a methylene group between the phenyl ring and acrylamide to increase the length of warhead. However, compound **10c** (R_1 = 5-Me) displayed a ~3-fold reduced FGFR1 kinase inhibitory activity and ~7-fold reduced cellular potency compared to **10a**. When a methyl group was attached to the end of acrylamides, probably due to the weaker reactivity of warhead, compounds **10b** and **10d** exhibited significant decrease in potency relative to **10a**. Compound **10e** (R_1 = 6-F) also showed improved activities in cellular assays, while **10g** (R_1 = 5-Br) did not display obviously improved cellular potency. Additionally, to improve the solubility of inhibitors, we attached an acrylamide moiety containing a tertiary amine to the phenyl ring to afford compounds **10h**−**10j**. Compounds **10h** and **10j** showed better cellular activities compared to **10i**. When a bulkier morpholine ring was attached to the end of acrylamide, compound **10k** exhibited dramatically decreased potency in the enzymatic and cellular assays when compared to **10h**. Compound **10l** displayed significantly reduced cellular activity when an acrylamide was place at the *meta*-position of phenyl ring. Besides, compound **10m** containing an alkyl amine sidechain on the phenyl group showed ~5-fold less cellular potency relative to **10a**.

2.3. *Reactivity and stability of compounds in mouse whole blood*

To determine the reactivity of compounds containing α,β-unsaturated amide with glutathione (GSH), a set of compounds (**10a**−**c**, **10e** and **10g**−**m**) were incubated with GSH in nude mouse whole blood. The glutathione adduct could be generated in the presence of GSH and electrophiles, which was detected by LC−MS/MS. For compounds **10b**, **10c**, **10i** and **10k**, there was no glutathione adduct detected, indicating their insufficient reactivity. As shown in Fig. 5A, compounds (**10a**, **10e**, and **10g**) containing an acrylamide group generally showed relatively higher reactivity than compounds **10h** and **10j** containing a *N*,*N*-dimethylaminomethyl group at the β-position of acrylamide. Moreover, the introduction of a methyl group or a morpholine ring onto the β-position of acrylamide (**10b** and **10k**, respectively) and a methyl group onto to the N of acrylamide (**10c**) resulted in no observed GSH adducts. These results are consistent with the previous reports that the β-substituted acrylamide could significantly enhance the stability of nucleophilic attack[36,37]. In addition, the GSH reactivity was modulated not only by different covalent warheads but also the electronic effects of the connected phenyl ring. For *meta*-acrylamide analog **10l** and *para*-acrylamide analog **10m** with an alkylamino side chain, a higher tendency toward GSH adduction was observed. In Table 5, the activation energy (E_a, kcal/mol), which describes the intrinsic kinetic energy barrier for a reaction, was also included for reference, and it showed impressive accordance with the GSH reactivity. For example, we may find that the compounds without observed GSH adducts (**10b** and **10k**) indeed show higher energy barrier for activation.

We also evaluated the stability of acrylamide-containing compounds in nude mouse whole blood (Fig. 5B). The half-lives ($t_{1/2}$) of compounds **10a**, **10e**, **10g**, **10h**, **10i**, **10j**, and **10l** with an acrylamide group or substituted acrylamide group were in the range of 1.44−2.71 h (Supporting Information Table S1). For compounds **10m** ($t_{1/2}$ = 0.93 h) with a high GSH reactivity, its elimination was quite fast, indicating that the reactivity might

Table 3 SAR of substituents on the pyrazole moiety.

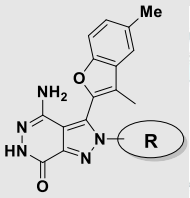

9a–9zb

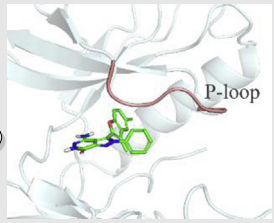

Compd.	R	FGFR1 IC_{50} (nmol/L)	Compd.	R	FGFR1 IC_{50} (nmol/L)
9a	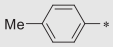	7.4 ± 1.0	**9o**	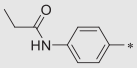	66.2%@0.1 μmol/L
9b		50.1 ± 21.8	**9p**		31.3 ± 2.8
9c	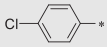	32.4 ± 6.2	**9q**		118.4 ± 12.0
9d	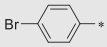	44.6 ± 0.9	**9r**	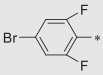	61.2%@0.1 μmol/L
9e	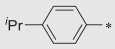	24.8 ± 1.1	**9s**	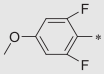	68.6%@0.1 μmol/L
9f	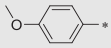	36.6 ± 7.7	**9t**		78.7%@0.1 μmol/L
9g	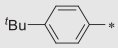	77.3%@0.1 μmol/L	**9u**	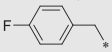	23.1%@0.1 μmol/L
9h		53.1 ± 6.9	**9v**	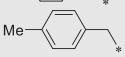	41.6%@0.1 μmol/L
9i	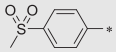	44.8 ± 10.7	**9w**	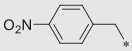	16.9%@0.1 μmol/L
9j	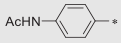	76.4%@0.1 μmol/L	**9x**	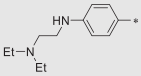	37.8%@0.1 μmol/L
9k	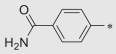	74.7%@0.1 μmol/L	**9y**	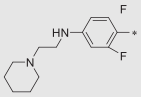	72.8%@0.1 μmol/L
9l	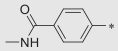	64.0%@0.1 μmol/L	**9z**	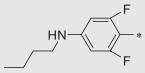	73.9%@0.1 μmol/L
9m	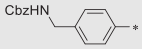	13.8 ± 1.3	**9za**	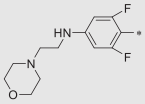	42.9%@0.1 μmol/L
9n	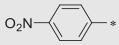	44.7 ± 2.2	AZD4547	—	0.8 ± 0.1

Values are the mean ± SD of two independent assays. –Not applicable.

contribute mainly to the consumption in whole blood. In contrast, the compounds **10k** ($t_{1/2}$ = 26 h), **10b** ($t_{1/2}$ = 71.2 h) and **10c** ($t_{1/2}$ = 72.9 h) showing less liability toward GSH were stable in whole blood. But beyond all that, the other compounds revealed more varied stability values and less evident relationship with structures or activation energy values, for which the stability might be also influenced by binding with other endogenously reactive components like plasma proteins[38–40].

Interest in drugs that covalently binds to and thus silences the target is driven by the desire for enhanced efficacy and selectivity by targeting uniquely positioned nucleophilic residues[41]. Taking both reduced risk of toxicity and *in vivo* efficacy into consideration, it is of high importance to balance the reactivity and stability of the covalent reactive groups. For compounds with relatively high GSH reactivity (**10m**, **10l** and **10e**), there may be higher risks of promiscuous reaction and side effects. In contrast, for compounds without showing any GSH reactivity (**10b**, **10c**, **10i** and **10k**), their covalent on-target binding and *in vivo* efficacy may call into question. Consequently, compound **10h** was selected here for the followed PK study, which exhibited not only moderate reactivity toward GSH and stability, but also potent cellular activity.

2.4. *Kinase selectivity profile of **10h***

As compound **10h** presents high potency against FGFR kinase, we further investigated its inhibitory activities against other tyrosine kinases to determine the selectivity profile of **10h**. Proteins with exposed nucleophilic centers may influence the selectivity toward the target. As reported by Brameld and co-workers[27], for various

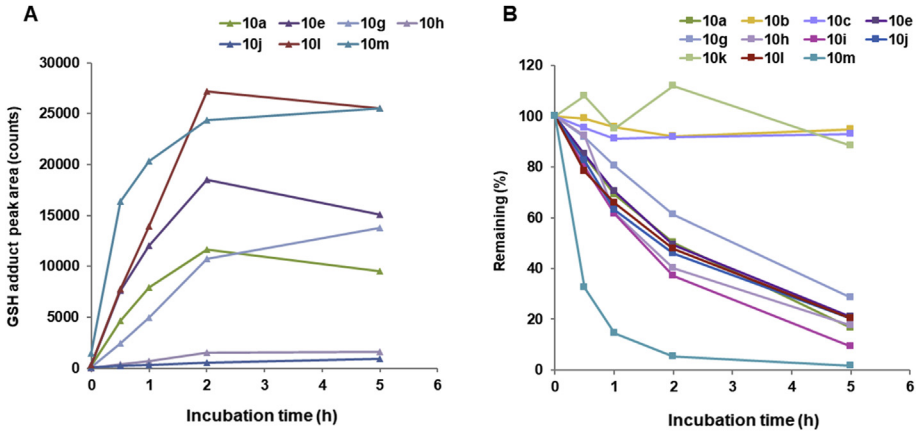

Figure 5 (A) Reactivity of compounds **10a**, **10e**, **10g**, **10h**, **10j**, **10l**, and **10m** with GSH in nude mouse whole blood. (B) The stability evaluation of compounds **10a**–**10c**, **10e**, and **10g**–**m** in nude mouse whole blood.

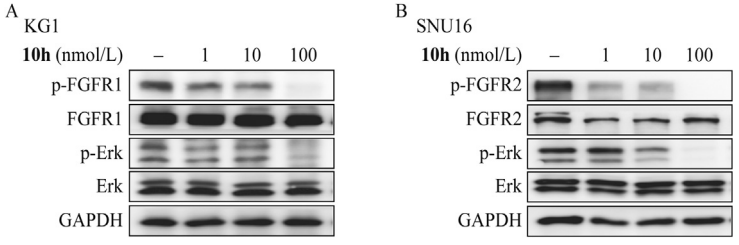

Figure 6 The effect of **10h** on phosphorylation of FGFR and downstream signaling molecules in KG1 and SNU16 cells.

kinases there mainly three cysteine residues are proximal to the ATP binding pocket, among which Cys488 (FGFR1 residue numbering) is conserved in less kinases. More importantly, Cys488 is not present in any of the closely related off-targets, such as VEGFR2(KDR), PDGFRα, or PDGFRβ. Considering our structure-based ligand design for covalent binding to Cys488 (Fig. 4), the kinase selectivity profile also supports that **10h** has achieved the desired selectivity. As shown in Table 6, Compound **10h** displayed highly potent inhibition activities against FGFR1, 2, 3, while it showed weak inhibition against FGFR4 (IC_{50} > 1000 nmol/L). Meanwhile, **10h** did not exhibit measurable inhibition (with IC_{50} > 1000 nmol/L) against these closely related off-target kinases, demonstrating significant selectivity over kinases with the cysteine lying on the other site (DFG-out pocket).

2.5. *Antiproliferative activity of **10h** on cancer cell lines*

In addition, we evaluated the antiproliferative potency of **10h** on several cancer cells with aberrant FGFR activation. As shown in Table 7, **10h** significantly inhibited the proliferation of FGFR1-translocated KG1 cells, FGFR2-amplified SNU-16 cells, and BaF3/TEL-FGFR4 cell lines with IC_{50} values of less than 1 nmol/L. **10h** also showed good antiproliferation activity of FGFR1-amplified H1581 cells (IC_{50} = 1.8 nmol/L). Additionally, **10h** exhibited potent activity against FGFR3-mutated UMUC14 cells (IC_{50} = 43 nmol/L). **10h** showed high cellular activity against BaF3/TEL-FGFR1 cell, while it did not dramatically inhibit the proliferation of BaF3/TEL-KDR cell. These results confirmed the high selectivity of **10h** for FGFR over KDR.

We also investigated the influence of **10h** on FGFR phosphorylation and its main downstream signaling molecules (Fig. 6). The results showed that **10h** significantly inhibited the phosphorylation of FGFR1 in KG1 and FGFR2 in SNU16 cell. The phosphorylation of ERK[42,43] was also inhibited in a dose-dependent manner by compound **10h**. These results indicated that **10h** could block cellular FGFR signaling pathway.

2.6. *PK study of compound **10h** in CD-1 mice*

With highly potent activities in biochemical and cellular assays, **10h** was chosen for PK study in CD-1 mice (Table 8). Following intraperitoneal (i.p.) and intravenous (i.v.) administration to CD-1

Table 4 Antiproliferative activity of selected compounds against SNU16 cancer cell lines.

Compd.	SNU16 IC_{50} (nmol/L)	Compd.	SNU16 IC_{50} (nmol/L)
8g	>1000	**9c**	31.4%@1 μmol/L
8h	>1000	**9e**	23.2%@1 μmol/L
8i	49.7%@1 μmol/L	**9i**	>1000
8m	>1000	**9z**	>1000
9a	>1000	AZD4547	3.7 ± 1.8

Values are the mean ± SD of two independent assays.

mice at doses of 3 and 1 mg/kg, respectively, **10h** displayed high exposure ($AUC_{0-\infty}$ = 704 ng/mL·h), high maximum concentration (C_{max} = 282 ng/mL, i.p.) and relatively rapid clearance (i.v.). The half-lives ($t_{1/2}$) of **10h** were 3.70 and 1.39 h, respectively, after both intraperitoneal and intravenous administration. The value of volume of distribution at steady state (V_{ss}) was 4819 mL/kg.

2.7. *In vivo antitumor efficacy of compound **10h***

To investigate antitumor activity of **10h** *in vivo*, a H1581 lung cancer xenograft mouse model was used, which featured FGFR1 amplified tumor context. As shown in Fig. 7A, **10h** suppressed tumor growth significantly in a dose-dependent manner compared to the vehicle group. The tumor weight inhibition rates of **10h** at the treatment endpoint were 91.6% and 74.4% at doses of 50 and 10 mg/kg, respectively (Fig. 7B). Besides, the tumor weight inhibition rate of AZD4547 (12.5 mg/kg) is 65.6%. Additionally, no obvious body weight loss was observed in all groups during the treatment (Fig. 7C). These results indicated that **10h** was a potent FGFR inhibitor with the potential for further development.

3. Conclusions

Several potent FGFR covalent inhibitors were obtained with the assistance of ligand-based virtual screening. Compound **10h** was obtained by SAR investigation with the guidance of molecular

Table 5 Biochemical activity and cellular activity of selected derivatives with an electrophile.

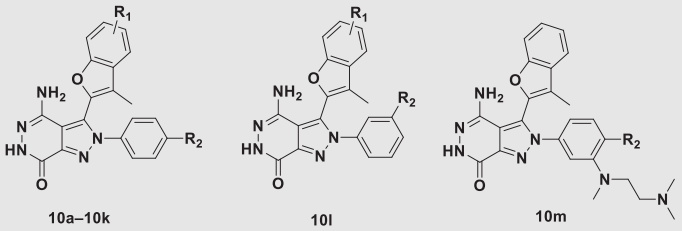

Compd.	R_1	R_2	FGFR1 IC_{50} (nmol/L)	SNU16 IC_{50} (nmol/L)	E_a (kcal/mol)
10a	5-Me		4.8 ± 1.6	2.5	4.86
10b	5-Me	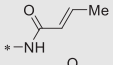	20.2%@0.01 μmol/L	–	9.38
10c	5-Me		16.3 ± 1.1	18.3	5.27
10d	5-Me	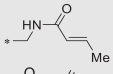	11.1%@0.01 μmol/L	–	–
10e	6-F		79	>1000	4.76
10f	7-MeO		27.2%@0.01 μmol/L	–	–
10g	5-Br		73.4%@0.01 μmol/L	37.0%@0.01 μmol/L	5.03
10h	5-Me	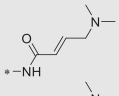	3	<0.3	5.47
10i	6-F	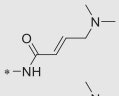	63.4 ± 3.6	>1000	5.67
10j	5-Br	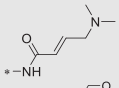	43.9%@0.01 μmol/L	8.2 ± 3.9	5.55
10k	5-Me	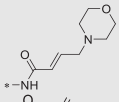	13.6%@0.01 μmol/L	75.7 ± 19.4	9.76
10l	5-Me		10.6%@0.01 μmol/L	660.4 ± 321.9	4.10
10m	5-Me		83.3 ± 11.9	12.2 ± 3.9	4.62
AZD4547			1.3 ± 0.3	3.7 ± 1.8	–

Values are the mean ± SD of two independent assays. E_a: the activation energy between the transition-state structure and the precursor molecule. –Not applicable.

Table 6 Kinase selectivity profile of **10h**.

Kinase	IC_{50} (nmol/L)	Kinase	IC_{50} (nmol/L)
FGFR2	1.9 ± 0.7	AXL	>1000
FGFR3	37.3 ± 2.5	Ret	>1000
FGFR4	>1000	DDR2	>1000
KDR	>1000	Met	>1000
VEGFR1	>1000	ALK	>1000
PDGFRα	>1000	c-Kit	>1000
PDGFRβ	>1000	Erk1	>1000
EGFR	>1000	Erk2	>1000
ErbB2	>1000	JAK1	>1000
ABL	>1000	JAK2	>1000
ErbB4	>1000	JAK3	>1000
c-Src	>1000	CDK1	>1000
IGF1R	>1000	CDK4	>1000
EPH-A2	>1000	CDK6	>1000

The data shown are mean values from two independent experiments.

docking, preliminary assessment of Michael acceptor chemical reactivity, pharmacokinetic properties, and antitumor activity in a xenograft model. **10h** remarkably inhibited proliferation of various cancer cells associated with FGFR dysregulation *via* suppressing FGFR signaling pathway. Moreover, **10h** displayed highly potent antitumor efficacy, causing tumor stasis at a dose of 50 mg/kg in the FGFR1-driven NCI-H1581 xenograft model. These results suggested that **10h** was a potential covalent FGFR inhibitor for further development.

4. Experimental

4.1. Molecular mechanics and DFT calculations

For the computational analysis of the differences in activation energy of the α,β-unsaturated amides, the model deprotonated nucleophile methane thiol was employed as surrogate for GSH. The molecules were prepared at pH 7.4 using LigPrep (LigPrep, version 4.6, 2019, Schrödinger, LLC., New York, NY, USA). Then, the conformational searches of ground states of reactants were performed with MacroModel (MacroModel, version 12.4, 2019, Schrödinger, LLC.) in water using the torsional sampling (MCMM) method and OPLS3 force field[44]. All the other parameters were remained as default values for molecular preparation and conformational search phases. The lowest energy conformer of each molecule was further optimized using Gaussian 09 software (Gaussian 09, 2009, Gaussian, Inc., Wallingford, CT, USA)[45]. Full geometry optimizations and frequency analyses of DFT calculations were carried out at the B3LYP/6-311+G (d, p) level. Harmonic vibrational frequencies were calculated for all stationary points using analytical gradients, confirming both true minima (no imaginary frequency) for the ground-state geometries of model nucleophile as well as for all 11 covalent-binding molecules. Transition-state optimizations were conducted for additions of MeS to the electrophilic β-carbon. The nature of stationary points was identified by means of frequency calculations for only one imaginary frequency of the respective electrophile−nucleophile reactions. The effect of bulk solvation was explored through optimization and single-point calculations using the solvation model density polarizable continuum model implemented in Gaussian 09[46]. Then, the reactive energy was calculated as the difference of single-point energy at the B3LYP/6-311+G (d, p) level between the reactants and corresponding transition state.

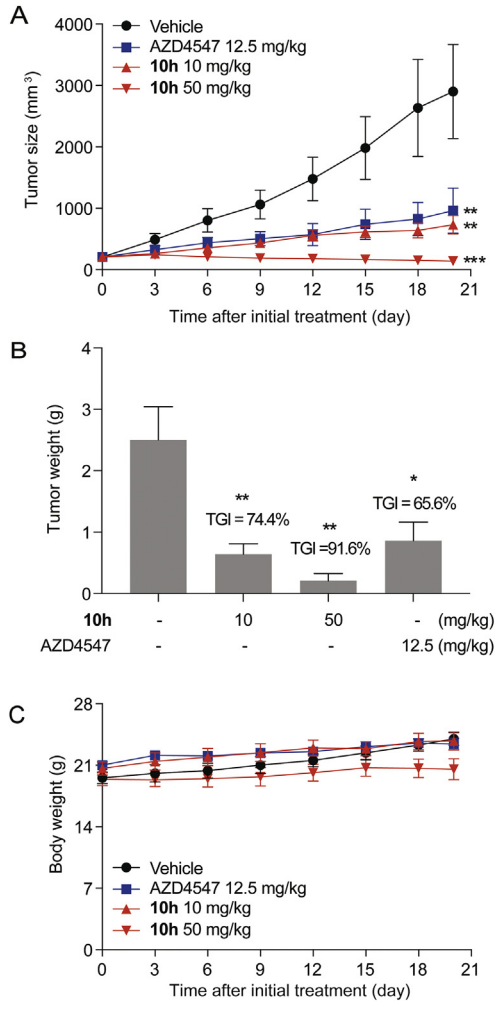

Figure 7 *In vivo* antitumor efficacy of compound **10h** in NCI-H1581 xenograft mouse model. The results are expressed as the mean ± SEM ($n = 6$ for per group) with $*P < 0.05$, $**P < 0.01$, $***P < 0.001$ *vs*. vehicle group determined by using One-Way ANOVA. (A) NCI-H1581 tumor xenografts were treated with **10h** (10 and 50 mg/kg once a day, i.p.) for 20 days after the tumor volume reached 180−220 mm^3. (B) Tumor weights of each group were measured on Day 20. (C) The changes of body weight during the treatment.

4.2. Chemistry

The chemical reagents from commercial sources were used without further purification. Preparative TLC (Qingdao Haiyang Chemical Co., Ltd., Qingdao, China) was 0.4−0.5 mm thickness. ^{1}H NMR and ^{13}C NMR spectra were recorded on a Bruker Avance III 400, 500 or 600 MHz spectrometer (Bruker Instruments, Inc., Ettlingen, Germany) with tetramethylsilane (TMS) as an internal standard. Chemical shifts were reported in parts per million (ppm, δ). Low-resolution mass spectra (LRMS) were obtained with a Finnigan LCQ Deca XP mass

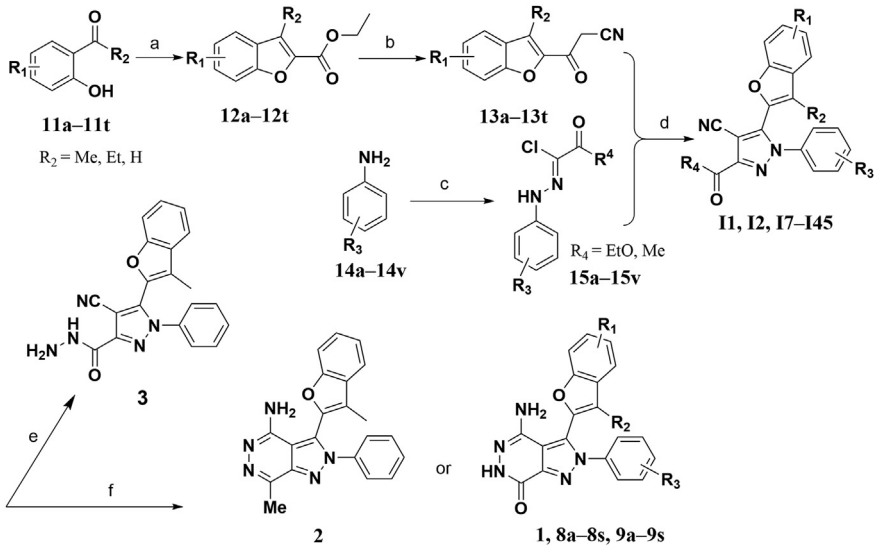

Scheme 1 Synthesis of compounds **1**–**3**, **8a**–**8s**, and **9a**–**9s**. Reagents and conditions: (a) ethyl bromoacetate, K_2CO_3, DMF, 100 °C; (b) CH_3CN, NaH, THF, 50 °C; (c) ethyl 2-chloroacetoacetate, $NaNO_2$, NaOAc, EtOH, H_2O/HCl (3:1, *v*/*v*), 0 °C–rt; (d) Et_3N, DCM, rt; (e) $N_2H_4{\cdot}H_2O$, HCl (conc.), EtOH, 80 °C; (f) $N_2H_4{\cdot}H_2O$, HCl (conc.), EtOH, 100 °C, microwave.

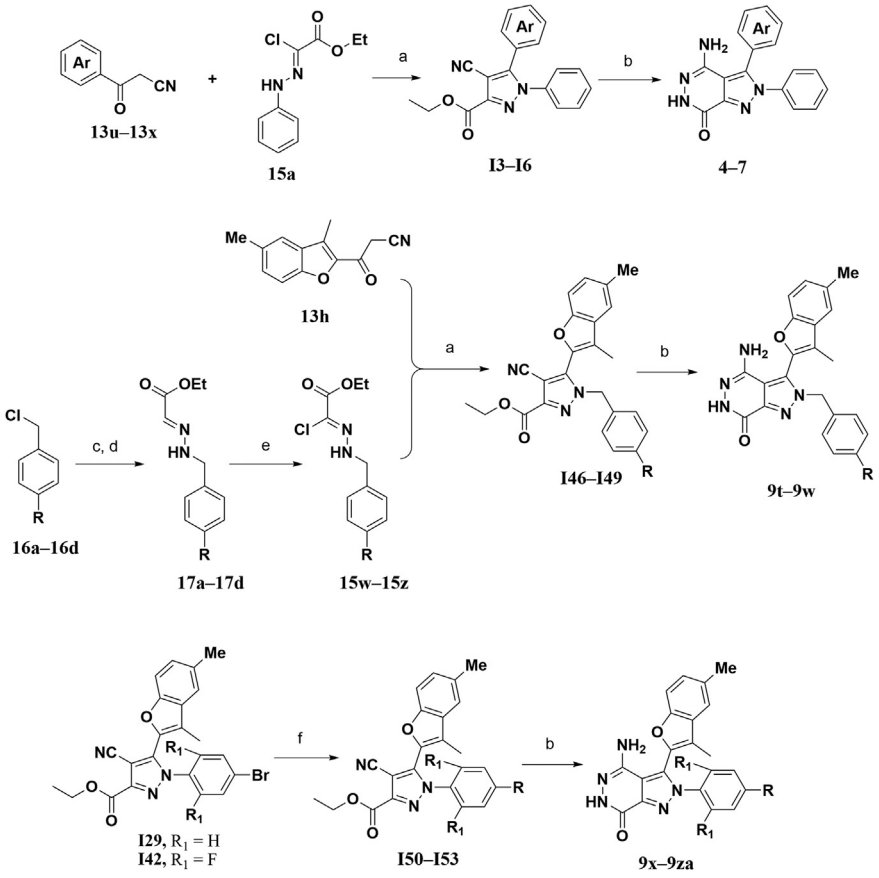

Scheme 2 Synthesis of compounds **4**–**7**, **9t**–**9w** and **9x**–**9za**. Reagents and conditions: (a) Et_3N, DCM, rt; (b) $N_2H_4 \cdot H_2O$, HCl (conc.), EtOH, 100 °C, microwave; (c) $N_2H_4 \cdot H_2O$, K_2CO_3, dioxane/H_2O (5:1, *v*/*v*), rt, 2 h; (d) ethyl glyoxylate, K_2CO_3, dioxane/H_2O, 50 °C, 5 h; (e) NCS, THF, rt–50 °C; (f) alkyl amines, $Pd_2(dba)_3$, BINAP, Cs_2CO_3, toluene, 110 °C, 36 h.

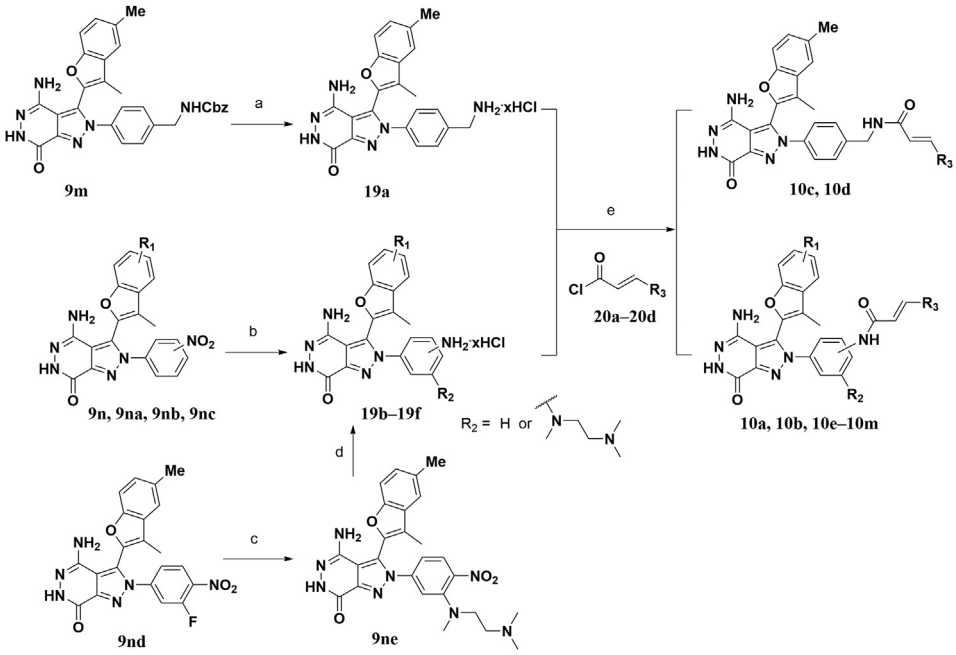

Scheme 3 Synthesis of compounds **10a**–**10m**. Reagents and conditions: (a) H_2 (1 atm), $Pd(OH)_2/C$, HCl (conc.), MeOH, 40 °C, 8 h. (b) Fe powder, HCl (conc.), MeOH/H_2O (6:1, *v*/*v*), 80 °C, 1 h; (c) *N*,*N*,*N*-trimethylethylenediamine, DIPEA, 90 °C, microwave, 2 h; (d) Fe powder, HCl (conc.), MeOH/H_2O (6:1, *v*/*v*), 80 °C, 1 h; (e) K_2CO_3, THF, rt.

Table 7 Anti-proliferation effects of **10h** on cancer cells.

Cell line	FGFR alteration	IC_{50} (nmol/L)	
		10h	AZD4547
KG1	FGFR1OP2-FGFR1	<0.3	3.7 ± 0.6
H1581	FGFR1 amplification	1.8 ± 0.4	59.8 ± 8.1
SNU16	FGFR2 amplification	<0.3	5.0 ± 0.1
UMUC14	FGFR3 mutation	43.0 ± 0.7	6.4 ± 1.3
BaF3/TEL-FGFR1	TEL-FGFR1	<0.3	0.5 ± 0.0
BaF3/TEL-KDR	TEL-KDR	>10,000	416.9 ± 10.0

Values are the mean ± SD of two independent assays.

Table 8 Pharmacokinetic profiles of compounds **10h** in CD-1 mice.

Compd.	Dose (mg/kg)	T_{max} (h)	C_{max} (ng/mL)	AUC_{0-t} (ng/mL·h)	$AUC_{0-\infty}$ (ng/mL·h)	MRT (h)	$t_{1/2}$ (h)	CLz (mL/min/kg)	V_{ss} (mL/kg)
10h (i.p.)	3	0.350	282	699	704	3.14	3.70	–	–
10h (i.v.)	1	–	–	281	321	1.36	1.39	65.2	4819

Experiments were conducted in male CD-1 mice ($n = 3$). Data are mean values.
–Not applicable.

spectrometer (San Jose, CA, USA). HRMS were measured on Micromass Ultra Q-TOF spectrometer (Milford, MA, USA). Compounds **1**, **8g**, **9n**, **10a**, **10c**, **10h**, **10j**, and **10k** were prepared in the same procedure[35]. All final compounds had an at least 95% purity. Due to the limited space of manuscript, general procedures and NMR data of the corresponding intermediates and all final products have been moved into the Supporting Information.

4.3. *Kinase inhibition assay*

The activity of Erk1, Erk2, JAK1, JAK2, JAK3, CDK1, CDK2 and CDK3 kinases was analyzed using the Z′-LYTE™ Kinase Assay Kit refer to the SelectScreen Kinase Profiling Service Z-lyte protocol. The other kinases activity was assessed using ELISA assay that performed in the same procedure as described in the previous report[35,47].

4.4. Whole blood stability assay

Stock solution of each test compound was prepared by dissolving the powder in dimethyl sulfoxide respectively and the final concentration was 10 mmol/L. Then the stock solution was diluted to obtain a working solution at 40 μmol/L in dimethyl sulfoxide. The fresh BALB/c nude mice (Beijing Vital River Laboratory Animal Technology Co., Ltd., Beijing, China. Laboratory Animal Management Department, Shanghai Institute of Planned Parenthood Research IACUC Issue No. 2019012) whole blood was prewarmed for 10 min at 37 °C in a thermomixer comfort (Eppendorf, Hamburg, Germany) prior to initiation of the reaction with each compound. The incubation mixture was composed of 312 μL fresh blood and 8 μL working solution, and the final concentration of each compound in the incubation mixture was 1 μmol/L. Following incubation, an aliquot of 50 μL of the incubation sample was removed at 0, 0.5, 1, 2 and 5 h, and quenched with 200 μL acetonitrile. The mixture was vortexed for 1 min and centrifuged at 12,000 rpm (centrifuge 5417R, Eppendorf) at room temperature for 10 min. 50 μL aliquot of supernatant was then transferred to a fresh 96-well plate, diluted with 50 μL acetonitrile/water (1:1, *v*/*v*), vortexed and centrifuged at 4000 rpm (centrifuge 5810R, Eppendorf) at room temperature for 10 min. Finally, aliquots of the diluted supernatant were subjected to LC−MS/MS analysis. All samples were prepared and analyzed in triplicates. For quantitative LC−MS/MS analysis, samples were separated using a Waters Acquity UPLC system (Milford, MA, USA) equipped with a Waters BEH C18 column (100 mm × 2.1 mm, 1.7 μm) at 45 °C. Eluates were analyzed using SCIEX API5000 triple quadrupole mass spectrometer (Toronto, Canada) with a TurboIonSpray interface. Chromatographic separation was done with a mobile phase composed of water with 0.1% formic acid (solution A) and acetonitrile/methanol (9:1, *v*/*v*) with 0.1% formic acid (solution B). The mobile phase was delivered at a flow rate of 0.4 mL/min, using a stepwise gradient elution program. In the MRM (multiple reaction monitoring) analysis, the source temperature was set at 550 °C, and the ionspray voltage was set to 5.5 kV. Mass spectrometry data was acquired and analyzed using AB Sciex Analyst version 1.6.2 software (Concord, Ontario, Canada). In addition, while monitoring the remaining amount of the parent compound, we also monitor the production of GSH adduct in the analysis samples. To improve the sensitivity of the GSH adduct screening, a MRM method in negative electrospray ionization mode was employed. The MRM transition targeting the GSH adduct was set from the $[M-H]^-$ to the product ion at *m*/*z* 272. The source temperature was set at 500 °C, and the ionspray voltage was set to −4.5 kV. The declustering potential was at −80 V, and the collision energy and spread in the negative mode were set at −40 and 10 eV, respectively. The data processing method for GSH adduct was the same as the parent.

4.5. Molecular modelling

For compound **1** the binding mode of the ligand and protein was simulated with the molecular docking program Glide (Glide, 2019, Schrödinger, LLC.). The ligand was prepared at pH 7.4 using LigPrep (LigPrep, version 4.6, 2019, Schrödinger, LLC.). The protein structure (PDB code: 6ITJ) was optimized by the module of Protein Preparation Wizard module at pH 7.4. The grid box was generated based on the ligand within the protein structure. Then, the prepared ligand was docked to the protein structure by Glide with Standard Precision mode. All the other parameters for above processes were the default parameters.

4.6. Western blot analysis

The cell signaling was detected by Western blot assay that performed in the same procedure as described in the previous report[35,47].

4.7. Cell proliferation assay

Cell proliferation was determined using a sulforhodamine B (SRB) assay or a cell counting kit (CCK-8) assay which performed as previously reported[35,47] or according to the manufacturer's specifications (Dojindo, Kumamoto, Japan).

4.8. Pharmacokinetic profiles in CD-1 mice

The PK properties were determined in CD-1 mice (5−6 weeks old, body weights range from 25.0 to 30.0 g. Beijing Vital River Laboratory Animal Technology Co., Ltd., Beijing, China. Laboratory Animal Management Department, Shanghai Institute of Planned Parenthood Research IACUC Issue No. 2019012, Shanghai, China), and all procedures relating to animal handling, care, and treatment were performed according to the guidelines approved by the Institutional Animal Care and Use Committee of the contract research organizations performing the study. Male CD-1 mice ($n = 3$ per group) was treated with a solution of compound **10h** (DMSO/Tween80/saline = 5/5/90, *v*/*v*/*v*) at doses of 3 and 1 mg/kg *via* intraperitoneal (i.p.) and intravenous (i.v.), respectively. Blood samples were collected at 0.05, 0.25, 0.75, 2, 4, 8, and 24 h after administration. Serum samples were obtained through common procedures and the concentrations of compound in the supernatant were analyzed by LC−MS/MS.

4.9. In vivo antitumor activity assay

All procedures relating to animal handling, care, and treatment were performed according to the guidelines approved by the Institutional Animal Care and Use Committee of the contract research organizations performing the study, IACUC Issue No. 20170909.

Female nude mice (5 weeks old, body weights range from 17.0 to 23.0 g, BALB/c, from Model Animal Research Center of Nanjing University, Nanjing, China) were housed and maintained under specific pathogen-free conditions. NCI-H1581 cells (1×10^6 in 200 μL, ATCC, Manassas, VA, USA) were injected subcutaneously (s.c.) into the right flanks of nude mice and allowed to grow to 700−800 mm^3, then cut into 27-mm^3 fragments and transplanted s.c. into the right flanks of nude mice using a trocar. When the tumor volume reached 180−220 mm^3, the mice were randomly assigned to vehicle and treatment groups randomly ($n = 6$ per group). The vehicle group received vehicle only, and the treatment groups received **10h** (5% Tween80 in sterile water for injection) *via* intraperitoneal administration once daily for 20 days. AZD4547 was a positive drug. The tumor volume (TV) was calculated as Eq. (1):

$$TV\ (mm^3) = (Length \times Width^2)/2\ . \quad (1)$$

The percentage of tumor growth inhibition values (TGI) was values were calculated on the final day of the study for the compound-treated mice and the vehicle-treated mice with Eq. (2):

$$\text{TCI}\ (\%) = 100\times\{1-[(V_{\text{Treated final day}}-V_{\text{Treated Day 0}})/(V_{\text{Control final day}}-V_{\text{Control Day 0}})]\} \quad (2)$$

Significant differences between the treated *versus* the control groups ($P \leq 0.05$) were determined using One-Way ANOVA.

Acknowledgments

We gratefully acknowledge financial support from the National Natural Science Foundation of China (81620108027 and 21632008 to Hong Liu, 81773634 to Mingyue Zheng and 81773762 to Jing Ai), National Science & Technology Major Project "Key New Drug Creation and Manufacturing Program" (2018ZX09711002, China), the Major Project of Chinese National Programs for Fundamental Research and Development (2015CB910304 to Hong Liu), "Personalized Medicines—Molecular Signature-based Drug Discovery and Development", and Strategic Priority Research Pro-gram of the Chinese Academy of Sciences (XDA12050201 to Mingyue Zheng, XDA12020000 to Meiyu Geng and XDA12020103 to Jing Ai). The Natural Science Foundation of China for Innovation Research Group (81821005 to Meiyu Geng, China). The Collaborative Innovation Cluster Project of Shanghai Municipal Commission of Health and Family Planning (2020CXJQ02 to Meiyu Geng, China).

Author contributions

Xiaowei Wu carried out synthesis experiments and analyzed spectral data and biological data of all compounds. Mengdi Dai, Xia Peng, and Yang Dai carried out kinase inhibition assays, cell proliferation assays. Rongrong Cui carried out whole blood stability assay. Yulan Wang, Jihui Zhao, and Tianbiao Yang performed molecular modelling and DFT calculation. Chunpu Li and Bao Wang assisted with synthesis experiments. Jing Ai, Mingyue Zheng, and Chunpu Li assisted in preparing manuscript. Hualiang Jiang, Meiyu Geng, Jing Ai, Mingyue Zheng, and Hong Liu designed and directed this project. Hong Liu and Xiaowei Wu co-wrote this manuscript with input from all authors.

Conflicts of interest

The authors declare no competing financial interest.

Appendix A. Supporting information

Supporting information to this article can be found online at https://doi.org/10.1016/j.apsb.2020.09.002.

References

1. Zhang J, Yang PL, Gray NS. Targeting cancer with small molecule kinase inhibitors. *Nat Rev Canc* 2009;**9**:28–39.
2. Wu P, Nielsen TE, Clausen MH. FDA-approved small-molecule kinase inhibitors. *Trends Pharmacol Sci* 2015;**36**:422–39.
3. Eswarakumar VP, Lax I, Schlessinger J. Cellular signaling by fibroblast growth factor receptors. *Cytokine Growth Factor Rev* 2005;**16**:139–49.
4. Turner N, Grose R. Fibroblast growth factor signaling: From development to cancer. *Nat Rev Canc* 2010;**10**:116–29.
5. Carter EP, Fearon AE, Grose RP. Careless talk costs lives: Fibroblast growth factor receptor signaling and the consequences of pathway malfunction. *Trends Cell Biol* 2015;**25**:221–33.
6. Heinzle C, Sutterlüty H, Grusch M, Grasl-Kraupp B, Berger W, Marian B. Targeting fibroblast-growth-factor-receptor-dependent signaling for cancer therapy. *Expert Opin Ther Targets* 2011;**15**:829–46.
7. Dieci MV, Arnedos M, Andre F, Soria JC. Fibroblast growth factor receptor inhibitors as a cancer treatment: From a biologic rationale to medical perspectives. *Canc Discov* 2013;**3**:264–79.
8. Wesche J, Haglund K, Haugsten EM. Fibroblast growth factors and their receptors in cancer. *Biochem J* 2011;**437**:199–213.
9. Dutt A, Salvesen HB, Chen TH, Ramos AH, Onofrio RC, Hatton C, et al. Drug-sensitive FGFR2 mutations in endometrial carcinoma. *Proc Natl Acad Sci U S A* 2008;**105**:8713–7.
10. Turner N, Pearson A, Sharpe R, Lambros M, Geyer F, Lopez-Garcia MA, et al. FGFR1 amplification drives endocrine therapy resistance and is a therapeutic target in breast cancer. *Cancer Res* 2010;**70**:2085–94.
11. Helsten T, Elkin S, Arthur E, Tomson BN, Carter J, Kurzrock R. The FGFR landscape in cancer: Analysis of 4,853 tumors by next-generation sequencing. *Clin Canc Res* 2016;**22**:259–67.
12. Katoh M. Therapeutics targeting FGF signaling network in human diseases. *Trends Pharmacol Sci* 2016;**37**:1081–96.
13. Ronca R, Giacomini A, Rusnati M, Presta M. The potential of fibroblast growth factor/fibroblast growth factor receptor signaling as a therapeutic target in tumor angiogenesis. *Expert Opin Ther Targets* 2015;**19**:1361–77.
14. Katoh M. Fibroblast growth factor receptors as treatment targets in clinical oncology. *Nat Rev Clin Oncol* 2019;**16**:105–22.
15. Nakanishi Y, Akiyama N, Tsukaguchi T, Fujii T, Sakata K, Sase H, et al. The fibroblast growth factor receptor genetic status as a potential predictor of the sensitivity to CH5183284/Debio 1347, a novel selective FGFR inhibitor. *Mol Canc Therapeut* 2014;**13**:2547–58.
16. Gavine PR, Mooney L, Kilgour E, Thomas AP, Al-Kadhimi K, Beck S, et al. AZD4547: An orally bioavailable, potent, and selective inhibitor of the fibroblast growth factor receptor tyrosine kinase family. *Cancer Res* 2012;**72**:2045–56.
17. Guagnano V, Furet P, Spanka C, Bordas V, Le Douget M, Stamm C, et al. Discovery of 3-(2,6-dichloro-3,5-dimethoxy-phenyl)-1-{6-[4-(4-ethyl-piperazin-1-yl)-phenylamino]-pyrimidin-4-yl}-1-methyl-urea (NVP-BGJ398), a potent and selective inhibitor of the fibroblast growth factor receptor family of receptor tyrosine kinase. *J Med Chem* 2011;**54**:7066–83.
18. Collin MP, Lobell M, Hübsch W, Brohm D, Schirok H, Jautelat R, et al. Discovery of rogaratinib (BAY 1163877): A pan-FGFR inhibitor. *ChemMedChem* 2018;**13**:437–45.
19. Perera TPS, Jovcheva E, Mevellec L, Vialard J, de Lange D, Verhulst T, et al. Discovery and pharmacological characterization of JNJ-42756493 (erdafitinib), a functionally selective small-molecule FGFR family inhibitor. *Mol Canc Therapeut* 2017;**16**:1010–20.
20. Futami T, Okada H, Kihara R, Kawase T, Nakayama A, Suzuki T, et al. ASP5878, a novel inhibitor of FGFR1, 2, 3, and 4, inhibits the growth of FGF19-expressing hepatocellular carcinoma. *Mol Canc Therapeut* 2017;**16**:68–75.
21. Zhao G, Li WY, Chen D, Henry JR, Li HY, Chen Z, et al. A novel, selective inhibitor of fibroblast growth factor receptors that shows a potent broad spectrum of antitumor activity in several tumor xenograft models. *Mol Canc Therapeut* 2011;**10**:2200–10.
22. Verstovsek S, Vannucchi AM, Rambaldi A, Gotlib JR, Mead AJ, Hochhaus A, et al. Interim results from Fight-203, a phase 2, open-label, multicenter study evaluating the efficacy and safety of pemigatinib (INCB054828) in patients with myeloid/lymphoid neoplasms

with rearrangement of fibroblast growth factor receptor 1 (FGFR1). *Blood* 2018;**132**:690.
23. Zhou W, Hur W, McDermott U, Dutt A, Xian W, Ficarro SB, et al. A structure-guided approach to creating covalent FGFR inhibitors. *Chem Biol* 2010;**17**:285−95.
24. Tan L, Wang J, Tanizaki J, Huang Z, Aref AR, Rusan M, et al. Development of covalent inhibitors that can overcome resistance to first-generation FGFR kinase inhibitors. *Proc Natl Acad Sci U S A* 2014;**111**:E4869−77.
25. Hagel M, Miduturu C, Sheets M, Rubin N, Weng W, Stransky N, et al. First selective small molecule inhibitor of FGFR4 for the treatment of hepatocellular carcinomas with an activated FGFR4 signaling pathway. *Canc Discov* 2015;**5**:424−37.
26. Brown WS, Tan L, Smith A, Gray NS, Wendt MK. Covalent targeting of fibroblast growth factor receptor inhibits metastatic breast cancer. *Mol Canc Therapeut* 2016;**15**:2096−106.
27. Brameld KA, Owens TD, Verner E, Venetsanakos E, Bradshaw JM, Phan VT, et al. Discovery of the irreversible covalent FGFR inhibitor 8-(3-(4-acryloylpiperazin-1-yl)propyl)-6-(2,6-dichloro-3,5-dimethoxyphenyl)-2-(methylamino)pyrido[2,3-*d*]pyrimidin-7(8*H*)-one (PRN1371) for the treatment of solid tumors. *J Med Chem* 2017;**60**:6516−27.
28. Joshi JJ, Coffey H, Corcoran E, Tsai J, Huang CL, Ichikawa K, et al. H3B-6527 is a potent and selective inhibitor of FGFR4 in FGF19-driven hepatocellular carcinoma. *Cancer Res* 2017;**77**:6999−7013.
29. Wang Y, Li L, Fan J, Dai Y, Jing A, Geng M, et al. Discovery of potent irreversible pan-fibroblast growth factor receptor (FGFR) inhibitors. *J Med Chem* 2018;**61**:9085−104.
30. Kalyukina M, Yosaatmadja Y, Middleditch MJ, Patterson AV, Smaill JB, Squire CJ. TAS-120 cancer target binding: Defining reactivity and revealing the first fibroblast growth factor receptor 1 (FGFR1) irreversible structure. *ChemMedChem* 2019;**14**:494−500.
31. Zhou Z, Chen X, Fu Y, Zhang Y, Dai S, Li J, et al. Characterization of FGF401 as a reversible covalent inhibitor of fibroblast growth factor receptor 4. *Chem Commun* 2019;**55**:5890−3.
32. Finlay MRV, Anderton M, Ashton S, Ballard P, Bethel PA, Box MR, et al. Discovery of a potent and selective EGFR inhibitor (AZD9291) of both sensitizing and T790M resistance mutations that spares the wild type form of the receptor. *J Med Chem* 2014;**57**:8249−67.
33. Miller VA, Hirsh V, Cadranel J, Chen YM, Park K, Kim SW, et al. Afatinib *versus* placebo for patients with advanced, metastatic non-small-cell lung cancer after failure of erlotinib, gefitinib, or both, and one or two lines of chemotherapy (LUX-Lung 1): A phase 2b/3 randomised trial. *Lancet Oncol* 2012;**13**:528−38.
34. Davids MS, Brown JR. Ibrutinib: A first in class covalent inhibitor of bruton's tyrosine kinase. *Future Oncol* 2014;**10**:957−67.
35. Wang Y, Dai Y, Wu X, Li F, Liu B, Li C, et al. The discovery and development of a series of pyrazolo[3,4-*d*]pyridazinone compounds as novel covalent FGFR inhibitors by rational drug design. *J Med Chem* 2019;**62**:7473−88.
36. Flanagan ME, Abramite JA, Anderson DP, Aulabaugh A, Dahal UP, Gilbert AM, et al. Chemical and computational methods for the characterization of covalent reactive groups for the prospective design of irreversible inhibitors. *J Med Chem* 2014;**57**:10072−9.
37. Jackson PA, Widen JC, Harki DA, Brummond KM. Covalent modifiers: A chemical perspective on the reactivity of α,β-unsaturated carbonyls with thiols *via* hetero-Michael addition reactions. *J Med Chem* 2017;**60**:838−85.
38. Ascenzi P, Fanali G, Fasano M, Pallottini V, Trezza V. Clinical relevance of drug binding to plasma proteins. *J Mol Struct* 2014;**1077**:4−13.
39. Wang J, Li-Chan XX, Atherton J, Deng L, Espina R, Yu L, et al. Characterization of HKI-272 covalent binding to human serum albumin. *Drug Metab Dispos* 2010;**38**:1083−93.
40. Dömötör O, Pelivan K, Borics A, Keppler BK, Kowol CR, Enyedy ÉA. Comparative studies on the human serum albumin binding of the clinically approved EGFR inhibitors gefitinib, erlotinib, afatinib, osimertinib and the investigational inhibitor KP2187. *J Pharmaceut Biomed Anal* 2018;**30**:321−31.
41. Zhao Z, Bourne PE. Progress with covalent small-molecule kinase inhibitors. *Drug Discov Today* 2018;**23**:727−35.
42. Liu H, Ai J, Shen A, Chen Y, Wang X, Peng X, et al. c-Myc alteration determines the therapeutic response to FGFR inhibitors. *Clin Canc Res* 2017;**23**:974−84.
43. Nakanishi Y, Akiyama N, Tsukaguchi T, Fujii T, Satoh Y, Ishii N, Aoki M. Mechanism of oncogenic signal activation by the novel fusion kinase FGFR3-BAIAP2L1. *Mol Canc Therapeut* 2015;**14**:704−12.
44. Harder E, Damm W, Maple J, Wu C, Reboul M, Xiang JY, et al. OPLS3: A force field providing broad coverage of drug-like small molecules and proteins. *J Chem Theor Comput* 2016;**12**:281−96.
45. Frisch MJ, Schlegel HB, Scuseria GE, et al. *Gaussian 09*. Wallingford, CT, USA: Gaussian, Inc.; 2009.
46. Marenich AV, Cramer CJ, Truhlar DG. Universal solvation model based on solute electron density and on a continuum model of the solvent defined by the bulk dielectric constant and atomic surface tensions. *J Phys Chem B* 2009;**113**:6378−96.
47. Ai J, Chen Y, Peng X, Ji Y, Xi Y, Shen Y, et al. Preclinical evaluation of SCC244 (Glumetinib), a novel, potent, and highly selective inhibitor of c-Met in MET-dependent cancer models. *Mol Canc Therapeut* 2018;**17**:751−62.